JACS
JOURNAL OF THE AMERICAN CHEMICAL SOCIETY
pubs.acs.org/JACS

Article

Ultrafast Proton Conduction in an Aqueous Electrolyte Confined in Adamantane-like Micropores of a Sulfonated, Aromatic Framework

Simon F. Winterstein, Alexei F. Privalov, Christopher Greve, Renée Siegel, Björn Pötzschner,[⊥] Michael Bettermann, Lea Adolph, Jana Timm, Roland Marschall, Ernst A. Rössler, Eva M. Herzig, Michael Vogel, and Jürgen Senker*

Cite This: J. Am. Chem. Soc. 2023, 145, 27563−27575

Read Online

ACCESS | Metrics & More | Article Recommendations | Supporting Information

ABSTRACT: Sulfonated, cross-linked porous polymers are promising frameworks for aqueous high-performance electrolyte-host systems for electrochemical energy storage and conversion. The systems offer high proton conductivities, excellent chemical and mechanical stabilities, and straightforward water management. However, little is known about mass transport mechanisms in such nanostructured hosts. We report on the synthesis and postsynthetic sulfonation of an aromatic framework (SPAF-2) with a 3D-interconnected nanoporosity and varying sulfonation degrees. Water adsorption produces the system SPAF-2^{H_2O}. It features proton exchange capacities up to 6 mequiv g^{-1} and exceptional proton conductivities of about 1 S cm^{-1}. Two contributions are essential for the highly efficient transport. First, the nanometer-sized pores link the charge transport to the diffusion of adsorbed water molecules, which is almost as fast as bulk water. Second, continuous exchange between interface-bound and mobile species enhances the conductivities at elevated temperatures. SPAF-2^{H_2O} showcases how to tailor nanostructured electrolyte-host systems with liquid-like conductivities.

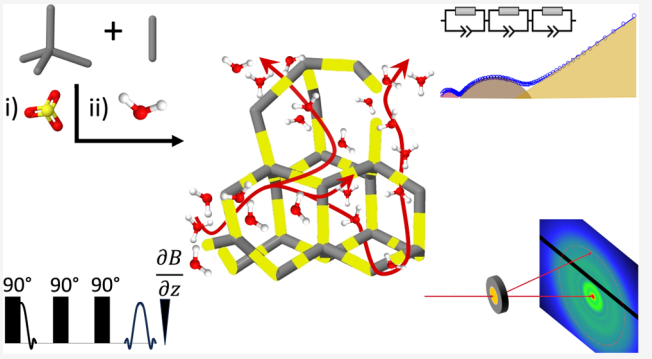

INTRODUCTION

Polymer electrolyte membrane fuel cells (PEMFCs) are promising devices for the sustainable conversion of chemically stored energy into electricity.[1] The active component of a PEMFC is the membrane-electrode assembly (MEA).[2] It consists of electrically conductive carbon black that is coated with platinum nanoparticles serving as catalysts for the oxidation of hydrogen and the reduction of oxygen on either side of the MEA.[1] The sandwiched proton-conducting membrane shuttles protons from the anode to the cathode, utilizing charge compensation and the water formation at the cathode. The membrane avoids the mixing of hydrogen and oxygen and minimizes electronic leakage currents.[3]

The state-of-the-art material for proton conductive polymer electrolyte membranes is Nafion.[4] It is a branched fluorinated copolymer with sulfonic acid groups at the side chain ends.[5,6] It features high ion exchange capacities (IECs) of about 1 mequiv g^{-1} and excellent proton conductivities up to 10^{-1} S cm^{-1} at 353 K and 100% relative humidity (RH).[6,7] As adsorbed water is attracted to the sulfonated side chains, water-rich channels are formed causing microphase separation.[5,8] The fluorinated, hydrophobic part provides the mechanical stability of the swollen membrane and serves as a confinement for the embedded water molecules and oxonium ions. The channels typically span several nanometers leading to moderate confinement effects on the dynamics and the transport properties of H_2O/H_3O^+.[5,9−13]

Low hydration levels favor vehicle transport, which facilitates charge transport by diffusion of oxonium ions.[9,14−16] Higher hydration degrees favor the Grotthus mechanism,[16−18] also referred to as the hopping or relay mechanism. Here, charge transport is mediated via protons that are transferred from water to water molecules.[19,20] This requires structural reorientation and displacement of water molecules to transfer protons from one water molecule to another. The transformation involves the formation of two clusters, the Zundel ($H_5O_2^+$) and the Eigen ($H_9O_4^+$) ions.[9,21,22] For systems with high proton densities it was suggested[19] that it is sufficient for the water molecules to perform small reorientations to enable the transfer of protons between oxonium ions and acid groups (pseudoshuttling).[20]

Nafion's water channels influence the transport mechanisms. The confinement, although moderate, creates a slightly higher

Received: August 24, 2023
Revised: November 12, 2023
Accepted: November 20, 2023
Published: December 7, 2023

https://doi.org/10.1021/jacs.3c09257
J. Am. Chem. Soc. 2023, 145, 27563−27575

Scheme 1. Synthesis of Tetrakis(4-bromophenyl)methane (BrTBPM) and Diboronic Acid (BDB) to PAF-2 and Subsequent Sulfonation to Sulfonated PAF-2 with a Sulfonation Degree x (SPAF-2$_x$)

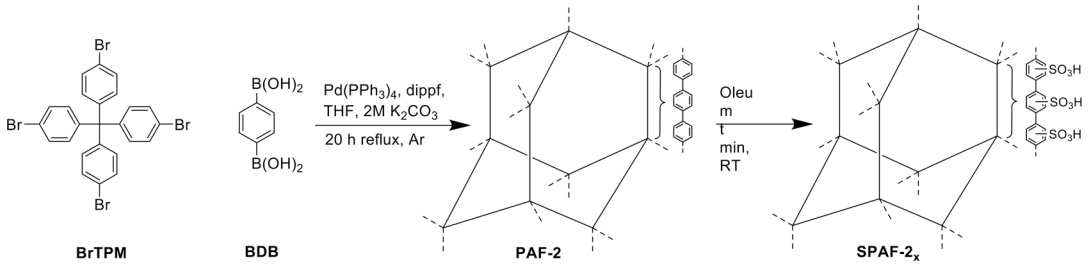

translational order for adsorbed molecules[12] and distorts the hydrogen bond network[13] typical for bulk water and distributes the motional modes[11] of the water molecules and oxonium ions. These dynamic heterogeneities include water molecules and oxonium ions strongly attracted to the sulfonic acid groups and free water in the inner part of the channels. While the former molecules are slowed down and restricted in their mobility, the latter ones diffuse freely in the channel interior.

Still, Nafion suffers from a limited working temperature up to 353 K as water is only weakly attached to the framework. This makes complicated water management necessary to avoid dissolution effects leading to a mechanical failure of the membranes.[5−8,23] Additionally, Nafions synthesis is expensive, and environmentally harmful products are formed during its long-term degradation.[6,24,25] This and the increasing demands for higher working temperatures and proton conductivities inspired the development of a variety of inorganic, organic, and hybrid materials that combine high proton conductivities with stronger retention forces for the water molecules. Promising material classes are polyoxometalates (POMs),[26] functionalized silicas,[27] metal−organic frameworks (MOFs),[26,28−30] porous organic frameworks (POFs),[31,32] covalent−organic frameworks (COFs),[26,33] and block copolymers.[34]

All of these materials have in common that they are micro- and/or mesoporous and feature an interconnecting pore structure. The strong host−guest interactions, typical for such systems, lead to higher water adsorption enthalpies, rendering the adsorbate molecules less likely to be desorbed at elevated temperatures. Table S1 shows that MOFs and COFs reach proton conductivities comparable to Nafion. Nevertheless, these systems often lead to powders composed of small particles.[17,26,35−40] This complicates the manufacturing of mechanically robust and gastight membranes. Mixed matrix membranes combine the mechanical stability of polymer membranes with the favorable properties of the porous particles.[5,17,23,41,42] The porous additives serve as reservoirs for both water and protons in turn easing the strong dependence of the proton conductivity on the hydration level and temperature pure Nafion membranes exhibit.

The small nanometer-sized cavities, typical for these materials, lead to strong confinement effects for the rotational and translational water dynamics.[43−47] If attractive forces prevail between the water molecules and the host surfaces, prominent effects are a slowdown of molecules close to the inner surfaces, leading to dynamic heterogeneities, and a reduction of the self-diffusion constants up to 3 orders of magnitude compared to bulk water.[43−45] If repulsive host−guest interactions or quantum-friction effects dominate, ultrafast water self-diffusion was reported in nanochannels.[46,47]

Up to now, mechanistic studies were carried out only for a few systems, and a general understanding of the underlying processes is missing. The chemical surface structure and related host−guest interactions become vitally important to establish efficient proton conduction paths.[34,48−51] High proton conductivities were observed when the functional surface groups were close enough to each other to shuttle protons[49,51] or allow for positioning of water molecules to form continuous hydrogen bond networks.[48,50,51] In both cases trains are induced along which protons are then transported without long-range mass transport as for Grotthuss-type mechanisms and pseudoshuttling.[19,20]

Here, we present a comprehensive study, investigating the synthesis, properties, and proton conductivities of aqueous electrolyte-host systems based on the sulfonated porous aromatic framework PAF-2.[35,52,53] Although PAFs are amorphous, they are often described in an idealized way by sp^3 carbon atoms positioned on a diamond-type lattice following the reticular synthesis concept.[32,54,55] These central units are connected along the four covalent bonds of the sp^3 carbon atoms by linkers consisting of linear chains of three (PAF-2) and two (PAF-1) benzene rings bonded via the 1,4-positions. Due to kinetic control, defects like one-sided linker termination and partial framework interpenetration are built into the frameworks, preventing long-range order. This leads to highly porous, amorphous materials with nanometer-sized 3D-interconnected adamantane-like pores.

The synthesis route allows for preparing sulfonated frameworks with high and varying sulfonation degrees (SPAF-2$_x$) without compromising the framework integrity. By combining electrochemical impedance spectroscopy (EIS), nuclear magnetic resonance (NMR) spectroscopy, and static-field gradient (SFG) NMR experiments, we investigated how the proton conductivity, the local mobility, and self-diffusion of H_2O/H_3O^+ are linked in nanoscale confinements that change as a function of the framework hydrophobicity, RH, and temperature. We provide intriguing insights into why sulfonated PAFs allow for liquid-like proton conductivities of up to 1 S cm^{-1}, in spite of the strong confinement, extending the suite of reported conduction mechanisms.

RESULTS AND DISCUSSION

Host System: SPAF-2$_x$. PAF-2 was synthesized following a protocol published by Kaskel and co-workers using tetrakis(triphenylphosphine)palladium(0) and diisopropylphosphineferrocene (dippf) as catalysts.[52] For gas-phase sulfonation, PAF-2 was exposed to an SO_3 atmosphere for 30, 90, and 180 s (Scheme 1).[35] The resulting products SPAF-2$_x$, where x denotes the sulfonation degree, were washed to remove nonbonded SO_3 molecules. We characterized all frameworks

https://doi.org/10.1021/jacs.3c09257
J. Am. Chem. Soc. 2023, 145, 27563−27575

by infrared (IR) and ^{13}C NMR spectroscopies, elemental analysis (EA), energy-dispersive X-ray spectroscopy (EDX), thermal gravimetric analysis (TGA), differential scanning calorimetry (DSC), Ar and H_2O physisorption, X-ray powder diffraction, and titration (Figures S1−S5 and Tables S2−S8). The resulting stoichiometries are given in Table 1.

Table 1. Average Stoichiometries and Sulfonation Degree x of PAF-2 and SPAF-2$_x$ from EA, EDX, and Titration[a]

sample	stoichiometry	$x = y/6$
PAF-2	$C_{37}H_{24}Br_{0.1}$	
SPAF-$2_{0.3}$	$C_{37}H_{22.2}(SO_3H)_{1.8}Br_{0.1} \cdot 0.5\ H_2O$	0.30
SPAF-$2_{0.5}$	$C_{37}H_{21.1}(SO_3H)_{2.9}Br_{0.2} \cdot 7.5\ H_2O$	0.48
SPAF-$2_{0.8}$	$C_{37}H_{19.3}(SO_3H)_{4.8}Br_{0.2} \cdot 4.5\ H_2O$	0.80

[a]Added water molecules are adsorbed in the framework. Additionally, small proportions of Pd (0.02 at %) and Fe (0.08 at %) were found. On average, they amount to 0.008 Pd and 0.03 Fe atoms to be added to the molecular formulas. For calculating the sulfonation degree $x = y/6$ the stoichiometries were rewritten as $C_1Ph_6(SO_3H)_yBr_z \cdot w\ H_2O$. Details of the evaluation are given in Tables S3−S7.

High cross-linking degrees of about 90% were determined for PAF-2. The remaining unconnected benzene rings are terminated with Br and small proportions of about 0.02 atom % palladium and 0.08 atom % iron were additionally detected. They are residuals of the used catalysts of the cross-coupling reaction and will occur most likely in an oxidized form as paramagnetic Pd^{2+} and Fe^{3+}. These impurities could not be removed by subsequent sulfonation and Soxhlet extraction, suggesting immobilization within the framework. The analyses show that the framework and residual Br end groups remain intact upon sulfonation and that the sulfonic acid groups are covalently attached to the framework's phenyl rings. The corresponding ^{13}C NMR resonances (Figure S1A) broaden markedly indicating that the $-SO_3H$ units are distributed over the 12 possible aromatic carbon atoms (C−H positions) of the three benzene rings of one rack. Together with the rotational freedom of the benzene rings, on average the SO_3H groups distribute over the inner pore surfaces.

The sulfonation degree $x = y/6$ (Table 1) for the three derivatives amounts to roughly 30, 50, and 80%. This corresponds to an average sulfonation of two, three, and five of the six phenyl rings of the repeating unit, for the likely case that only monosulfonation of the phenyl rings occurs. Moreover, IECs of 2.77 mequiv g^{-1} (SPAF-$2_{0.3}$), 4.12 mequiv g^{-1} (SPAF-$2_{0.5}$), and 5.67 mequiv g^{-1} (SPAF-$2_{0.8}$) were derived, which exceed the IEC of Nafion by up to six times.[38] The accessible amount of SO_3H units calculated from the IECs matches the stoichiometries, demonstrating that all sulfonic acid groups point into the pores and are accessible to adsorbed water molecules. Thus, all sulfonic acid groups will contribute to the proton conductivity of SPAF-2 derivatives (see below). Neither the structural integrity nor the sulfonation degree changed during the temperature-dependent EIS and NMR spectroscopic measurements demonstrating the long-term stability of the sulfonated frameworks. This was shown by repeated ^{13}C NMR and IR spectroscopic (Figure S1A,D), and titration experiments (Figure S3 and Table S7).

Decomposition of SPAF-2$_x$ (x = 0.3, 0.5, 0.8) sets in above 485 K (Figure S1C). At this temperature, the frameworks start to lose the attached sulfonic acid groups, as shown by coupled thermogravimetric analysis and mass spectrometry (TGA-MS) experiments (Figure S4). As such, all SPAF-2$_x$ derivatives should be stable even under harsh conditions in high-temperature PEMFC that work around 450 K.

As previously reported, PAF-2 exhibits a remarkable micro- and mesoporosity with highly interconnected pore spaces (Figures S1B and S2).[52,56] The Brunauer−Emmett−Teller (BET) surface area (Ar) and total pore volume amount to 1690 $m^2\ g^{-1}$ and 1.20 $cm^3\ g^{-1}$ (Table 2). About 50% of the total pore volume results from micropores with a maximum pore width of roughly 1 nm. The surface area and pore volume are roughly 20% larger than previously reported.[52,57] We attribute this to a higher cross-linking degree. The hysteresis for the desorption branch of the isotherm suggests a moderate capability to swell, which is probably caused by the remaining unconnected end groups allowing for a certain flexibility.[52] Furthermore, the magnitudes of the observed surface areas, pore volumes, and narrow pore size distributions suggest partial framework interpenetration.[54,55] Sulfonation causes severe decreases in both surface area and pore volume. For SPAF-$2_{0.3}$ roughly 20% of the original pore volume remains accessible to Ar, while it is further reduced to about 10% for SPAF-$2_{0.8}$. This is accompanied by a decrease in the micropore fraction, indicating that preferentially micropores contract upon sulfonation due to the strong increase in multipole interactions between neighboring SO_3H units.

Due to kinetic control for PAF-2 synthesis, all frameworks are amorphous (Figure S1E).[32,54,55] Their X-ray powder patterns share broad maxima at 17°, 23°, and 43° in 2Θ, suggesting that characteristic framework distances and topology do not change upon sulfonation. The observed intensity modulations are most likely caused by attaching sulfonic acid groups to the benzene rings. These results align with the ^{13}C MAS and IR spectroscopic analyses (Figure S1). Previous studies propose that the flexibility introduced by the remaining dangling bonds favors framework deformation and partial interpenetration, preventing the formation of long-range order. Nevertheless, locally, the frameworks will consist of connected adamantane-type units.

Electrolyte-Host System: SPAF-2$_x^{RH}$. The water isotherm of PAF-2 (Figure 1A) shows the expected behavior (type V according to IUPAC classification)[56] of a hydrophobic framework. The water gate-opening partial pressure occurs at

Table 2. Ar Surface Areas, Total Pore Volume, and Micropore Ratio of PAF-2 and SPAF-2$_x$

sample	BET SA(Ar) /$m^2\ g^{-1}$[a]	DFT SA(Ar)/$m^2\ g^{-1}$[b]	pore volume/cc g^{-1}[b]	micropore ratio/%[b]
PAF-2	1692	1761	1.263	48
SPAF-$2_{0.3}$	352	380	0.271	46
SPAF-$2_{0.5}$	136	153	0.25	17
SPAF-$2_{0.8}$	124	123	0.198	19

[a]Calculated using the BET equation. [b]Derived using an equilibrium model for a quenched solid density functional theory (QSDFT) slit-pore kernel (Ar at 87 K on carbon).

https://doi.org/10.1021/jacs.3c09257
J. Am. Chem. Soc. 2023, 145, 27563−27575

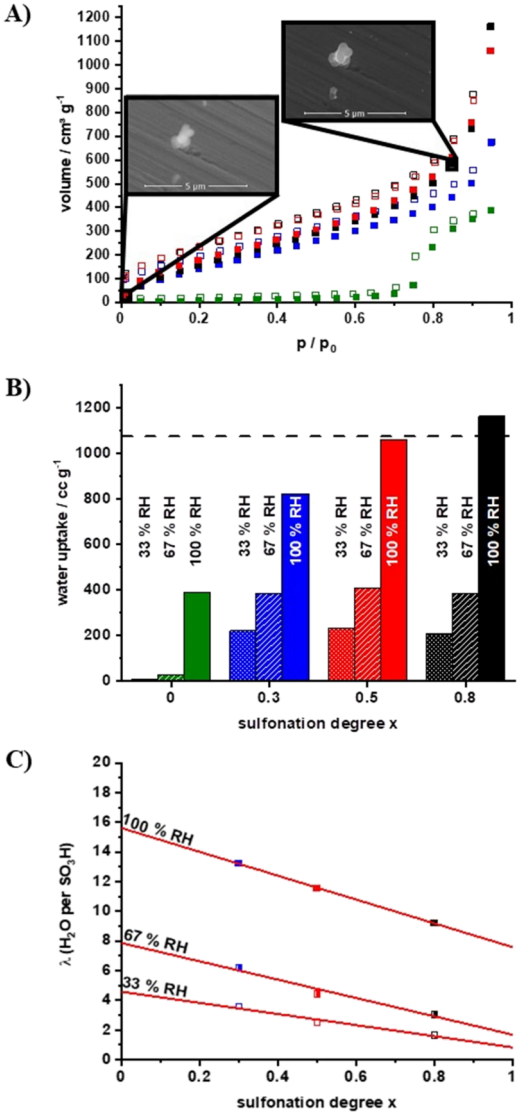

Figure 1. Water adsorbed in PAF-2 (green) and SPAF-2$_x$ (x = 0.3 (blue), 0.5 (red), and 0.8 (black)). (A) H_2O isotherms measured at 293 K for PAF-2 and SPAF-2$_x$. SEM images obtained for SPAF-$2^{RH}_{0.8}$ at 1.3% RH and 89.9% RH are included as insets. (B) Water uptake at 33% RH (dotted), 67% RH (shaded), and 100% RH (full) derived from the water isotherms. The horizontal dashed line indicates when the original pore volume of PAF-2 would be filled with H_2O molecules. The volume is derived from the Ar uptake of PAF-2 assuming that H_2O and Ar follow the ideal gas equation (Figure S1B). (C) Number of water molecules per SO_3H group (λ) determined from the water isotherms at 33, 67, and 100% RH.

a RH of 70%. Below this value, water is repelled but adsorbs readily at higher RH. At 100% RH, PAF-2 takes up roughly 390 cm^3 g^{-1}. Sulfonation makes the materials remarkably hydrophilic (Figure 1B). For SPAF-2$_x$, the water adsorption starts at low RH and continuously increases to values of 820 cm^3 g^{-1} (x = 0.3), 1060 cm^3 g^{-1} (x = 0.5), and 1160 cm^3 g^{-1} (x = 0.8) at 100% RH. This corresponds to an enhancement of the water uptake by 2 and 3 for 100% RH. However, the enhancement factors are on the order of a few hundred below the gate-opening RH of PAF-2.

In the latter regime, the water uptake depends markedly on the RH but is hardly affected by the sulfonation degree (Figure 1B). We attribute this to the strong retention forces caused by the attractive interactions between the deprotonated sulfonic acid groups and the H_3O^+ ions. In contrast, the framework retention caused by the SO_3H groups is overcome for high RH, rendering the framework contraction (Table 2) reversible. The contracted pores reopen, regenerating the originally accessible pore volume (Figure 1B). Thus, the adsorbed H_2O molecules and H_3O^+ ions move more freely in the pore system. For 100% RH, the water uptake saturates for x > 0.5. This is accompanied by an increase of the particle sizes of about 10% as observed in environmental scanning electron microscopy (Figure 1A). In turn, the pore sizes and alignment of the framework racks are influenced by the water uptake.

DSC measurements for SPAF-2$_x$ (Figure S5) reveal freezing and melting peaks during the cooling−heating cycle for 100% RH. The onset temperature of about 245 K (heating branch) is typical of ice melting in mesopores with average diameters smaller than 5 nm.[58] Based on the total water uptake (Figure 1B) and the molar melting enthalpy of ice[59] the freezable water fraction amounts to less than 15%. As the melting enthalpy might be changed in confined spaces, we regard the obtained freezable water fraction as the upper boundary. For 33 and 67%, no freezing and melting peaks were observed. Thus, in all cases, >85% of the water is adsorbed in confinements where water does not freeze and thus remains mobile for temperatures well below 273 K. This is promising for low-temperature applications. Transient water clusters and hydrogen bond networks typical for bulk water will be suppressed or distorted, rendering the formation of Zundel and Eigen ions needed for a Grotthus-type proton transport unlikely. By contrast, the water in the larger channels of Nafion is susceptible to crystallization.[5,60]

Considering that the water molecules are stored in micropores and subordinated in small mesopores, it is plausible that the water uptake is limited. We observed saturation for 100% RH and high sulfonation degree x (Figure 1B). Intriguingly, an equivalence of the molar volumes for water molecules adsorbed in SPAF-2$_x$ and Ar in PAF-2 was found, which suggests that the pore volume of PAF-2 is retrieved upon water adsorption. As the maximum amount of water is limited, increasing x leads to higher H_3O^+ concentrations. The number of water molecules per SO_3H group λ (Figure 1C) decreases linearly as a function of x. Roughly 13 water molecules are matched with one $-SO_3H$ group for x = 0.3 and λ reduces to about 9 water molecules for x = 0.8, given that both samples are saturated at 100% RH. Lowering RH led to significantly lower λ values down to λ = 2, while preserving the general trend. The opposite behavior (increasing λ with rising x) was observed for materials like Nafion 117 and SPAF-1,[35,61] where the water uptake is driven by solvation of the SO_3^- and H_3O^+ ions and not by the free adsorption volume available to the water molecules. At 100% RH λ of Nafion 117 and SPAF-$2^{100}_{0.3}$ are similar.[61]

SPAF-2^{RH}_x show some important characteristics. They take up roughly their own weight in water (e.g., 48 wt % of water for SPAF-$2^{100}_{0.8}$) without losing the framework integrity or changing phase and shape, which is advantageous compared to common exchange membranes.[62] Due to the large IECs (up to 5.7 mequiv g^{-1}), a fluid with a high proton concentration is created in 3D pores, which promises high proton conductivities for SPAF-2^{RH}_x derivatives. As the water molecules are mainly confined to the microporous spaces, they exhibit strong host−guest interactions and are less likely to be desorbed

https://doi.org/10.1021/jacs.3c09257
J. Am. Chem. Soc. 2023, 145, 27563−27575

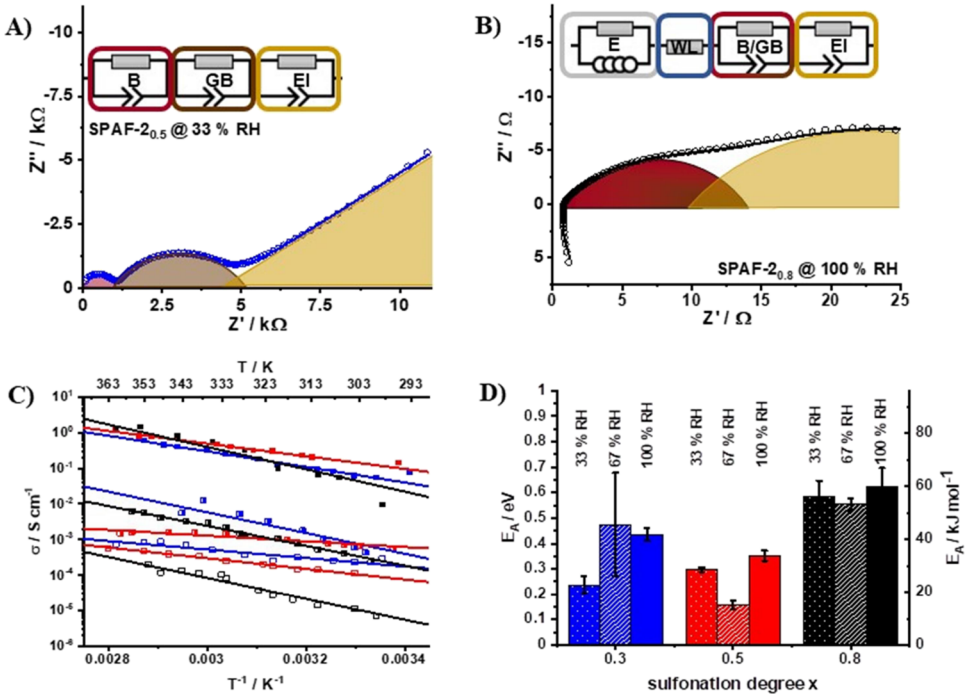

Figure 2. EIS measurements, conductivities, and activation barriers of SPAF-2_x^{RH}. (A) Nyquist plot of SPAF-$2_{0.5}^{33}$ at 303 K with an equivalent circuit containing RC elements for bulk in dark red (B), grain boundaries in brown (GB), and electrode interface in yellow (EI). (B) Nyquist plot of SPAF-$2_{0.8}^{100}$ at 306 K with the equivalent circuit consisting of elements for electrodes and cables in gray (E), a water film in blue (WL), bulk and grain boundaries in dark red/brown (B/GB), and an electrode interface in yellow (EI). (C) Arrhenius plot of σ for SPAF-$2_{0.3}$ (blue), SPAF-$2_{0.5}$ (red), and SPAF-$2_{0.8}$ (black) for various relative humidities. Empty, half-filled, and filled symbols correspond to 33, 67, and 100% RH, respectively. While σ for 33 and 67% RH are bulk conductivities, the ones for 100% RH are joint bulk and grain boundary conductivities (Tables S10−S21). (D) Activation barriers for various sulfonation degrees and relative humidities.

compared to Nafion. As such, SPAF-2_x^{RH} offer less demanding water management for polymer fuel cell applications.

Proton Conductivity of SPAF-2_x^{RH}. EIS on pellets pressed from SPAF-2_x^{RH} powders revealed two main regimes. SPAF-$2_{0.3}^{RH}$ and SPAF-$2_{0.5}^{RH}$ equilibrated at 33 and 67% RH exhibited three half-circles in the Nyquist plots (Figures 2A, S9, S10, S13, and S14), which were well described by three RC elements in series. The capacities of the three RC elements in the equivalent circuit are characteristic for (i) bulk conduction ($<C> \approx 10^{-12}$ F), (ii) transport over the grain boundaries ($<C> \approx 10^{-7}$ F), and (iii) polarization and chemical reactions at the electrodes ($<C> \approx 10^{-4}$ F). As H^+/H_3O^+ are the only mobile charge carriers, we attribute the first two elements to the conduction of protons in the pore system of the individual SPAF-2_x^{RH} particles and the transport between the particles. The corresponding resistances R serve as a measure for DC conductivities σ_B and σ_{GB}.

The proton bulk conductivities σ_B in this regime reach values between 10^{-5} and 10^{-2} S cm^{-1} (Figure 2C) and exhibit an Arrhenius temperature dependence. Proton conduction over the grain boundaries σ_{GB} is on average 2 orders of magnitude lower (Tables S10, S11, S14, and S15). Retarded proton transport between particles implies that the water molecules and oxonium ions are effectively confined to the SPAF-2_x^{RH} particles. The RH has a strong influence on the σ_B (Figure 2C). Equilibrating the samples at 67% instead of 33% RH enhances σ_B by up to 2 orders of magnitude. We attribute this to the larger number of water molecules per SO_3H unit (Figure 1C). The additional water improves the oxonium ion solvation, separates H_3O^+/SO_3^- ion pairs more efficiently, and thus allows part of the framework porosity to be restored. In turn, the mobility of the water molecules and oxonium ions increases.

In contrast, changing the sulfonation degree from 0.3 to 0.5 has only minor effects on σ_B (Figure 2C). This is unexpected, as the IEC almost doubles. Due to the strong confinement, the water uptake is limited by strong retention forces of the ion pairs, trapping H_3O^+ ions within the vicinity of the sulfonic acid groups. Increasing the temperature from RT to 353 K improves σ_B by roughly 1 order of magnitude. The activation barriers (E_A) for the thermally activated conduction are similar (Figure 2D) and vary between 30 and 40 kJ mol^{-1}. H^+ transport with E_A in this regime is typically considered as borderline between Grotthuss and vehicle mechanisms.[19,63,64]

The impedance spectra for SPAF-$2_{0.8}^{RH}$, SPAF-$2_{0.5}^{100}$, and SPAF-$2_{0.3}^{100}$ change markedly (Figures S11, S15, S17−S19). As the overall resistance is quite low in this regime, an equivalence circuit for the electrode was added to the refinements (Figure 2B). More importantly, the equivalence circuits for the bulk and the grain boundaries merge into one circuit as only one relaxation process is resolved in the distribution of relaxation times (Figure S6B) in addition to the electrode and electrode interface elements. This suggests that the protons and oxonium ions exchange freely between the pore volumes of the SPAF-2_x^{RH} particles and the grain boundary regions. This is intriguing, as it suggests that SPAF-2_x^{RH} derivatives, in particular when saturated at 100% RH, might be used as fuel cell separators without the need to prepare a homogeneous film as long as the hydrogen and oxygen gas permeabilities are low enough for the dense particle films. In particular, as the SPAF-2_x^{RH} electrolyte-host systems are long-term stable, shown by the EIS measurements repeated after several months.

https://doi.org/10.1021/jacs.3c09257
J. Am. Chem. Soc. 2023, 145, 27563−27575

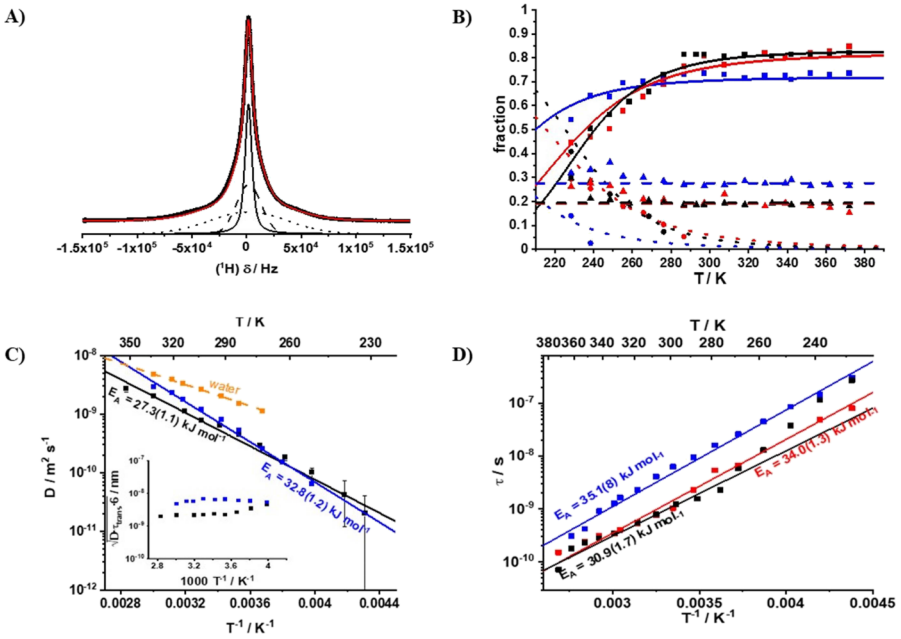

Figure 3. NMR spectroscopic studies of SPAF-2_x^{100}. (A) ^{1}H NMR spectrum of SPAF-$2_{0.8}^{100}$ at 224 K (black dots). The spectrum was fitted (red solid line) superimposing three signals representing mobile water (black solid line, fwhm < 10 kHz), framework (black dashed line, fwhm ≈ 27 kHz), and bound water (black pointed line, fwhm ≈ 81 kHz). (B) Proportion of protons of the mobile (squares, solid line) and immobile (circles, pointed line) H_2O/H_3O^+ and of the framework (triangles, dashed lines) derived from the line shape analyses of the ^{1}H NMR spectra of SPAF-$2_{0.3}^{100}$ (blue), SPAF-$2_{0.5}^{100}$ (red), and SPAF-$2_{0.8}^{100}$ (black) (Figures S22−S24 and Table S22). The solid and pointed lines are refinements of eq 1. (C) Self-diffusion coefficients D from SFG NMR experiments for SPAF-2_x^{100} [x = 0.3 (blue), 0.8 (black)] and liquid water (orange).[66] The inset of panel (C) shows the square root of $6D\tau_{trans}$ for SPAF-$2_{0.3}^{100}$ (blue) and SPAF-$2_{0.8}^{100}$ (black). (D) Correlation times τ_{trans} for the H_2O/H_3O^+ translation calculated from T_1 measurements of SPAF-2_x^{100} [x = 0.3 (blue), 0.5 (red), and 0.8 (black)].

For a RH of 100%, $\sigma_{B/GB}$ rises by roughly 2 orders of magnitude with only a moderate dependence of $\sigma_{B/GB}$ on the sulfonation degree. At about 353 K, $\sigma_{B/GB}$ varies between 1.4 S cm^{-1} for SPAF-$2_{0.8}^{100}$ and 0.6 S cm^{-1} for SPAF-$2_{0.3}^{100}$ (Tables S12, S16 and S20). These conductivities are about four decades higher compared to PAF-2 (Figure S7), outperforming those of Nafion[61] by roughly 1 order of magnitude and approach the values for liquid electrolytes[65] with the advantage of SPAF-2_x^{RH} not losing the form stability. One reason for the exceptionally high conductivities might be the open 3D pore structure of the framework,[32,53] which enables oxonium ions and water molecules to move essentially unrestricted through the pore structure as previously suggested for SPAF-1.[35] Immersing SPAF-$2_{0.3/0.5/0.8}$ in liquid water led to slightly lower conductivities (Figure S21), which probably is a consequence of inhomogeneous pore filling. Thus, we focus on gas-phase equilibration for preparing the electrolyte-host system SPAF-2_x^{RH}.

While the conductivities at ambient temperatures are similar for all three sulfonation degrees at 100% RH, the activation barriers differ significantly. For x = 0.8, E_A is the largest with 59 kJ mol^{-1}, goes through a minimum at x = 0.5 (E_A ≈ 35 kJ mol^{-1}), and increases slightly for x = 0.3 (E_A ≈ 43 kJ mol^{-1}). Similar trends were also observed for 67 and 33% RH. The observation that E_A is the largest (≈60 kJ mol^{-1}) for x = 0.8, independently of RH, indicates that the high SO_3^- density introduces confinement effects, which influence the proton conductivity in all cases. Low sulfonation degrees of 30%, however, lead to low charge carrier concentrations and a reduced ability of the frameworks to swell upon water uptake. Consequently, the confinement changes, and oxonium ions and the water molecules within the pores are more strongly affected by the negative framework charge. Optimal values of charge density, carrier concentration, water uptake, and framework swelling appear to be reached for medium sulfonation degrees of around x = 0.5.

Counterintuitively, the charge transport activation barriers do not change steadily with water uptake (Figure 2D). This can be explained, if more than one thermally activated process drives the charge transport. The corresponding E_A will exhibit different trends upon changing the confinement by adapting RH and x. To derive a better understanding of the nature of these processes temperature-dependent ^{1}H NMR spectroscopic line shape, spin−lattice relaxation, and SFG experiments were carried out for SPAF-$2_{0.3}^{100}$, SPAF-$2_{0.5}^{100}$, and SPAF-$2_{0.8}^{100}$.

H_3O^+/H_2O Mobility and Diffusion. At low temperatures (≈ 220 K), the lineshapes of the ^{1}H NMR spectra for SPAF-$2_{0.3}^{100}$, SPAF-$2_{0.5}^{100}$, and SPAF-$2_{0.8}^{100}$ consist of three distinctly different components (Figure 3A). Two components are broad and were fitted with Gaussian profiles. Their full widths at half-maximum (fwhm) were found to be about 27 and 81 kHz, independent of the temperature. The third component is Lorentzian-type and narrow, with fwhm <10 kHz. The Gaussian-type resonance with a fwhm of about 27 kHz is typical of a rigid SPAF-2 framework, where the shortest ^{1}H−^{1}H distances (d ≈ 2.4 Å) arise from neighboring protons at the aromatic rings. The fraction of this line shape component (dashed line, Figure 3A) is also temperature-independent (Figure 3B), indicating that the framework remains rigid between 220 and 380 K. The derived proportions (0.17 for SPAF-$2_{0.8}$, 0.18 for SPAF-$2_{0.5}$, and 0.28 for SPAF-$2_{0.3}$) match well the expected ^{1}H ratios for framework and water hydrogen atoms.

https://doi.org/10.1021/jacs.3c09257
J. Am. Chem. Soc. 2023, 145, 27563−27575

The two remaining resonances were assigned to adsorbed water molecules and oxonium ions. The broad Gaussian-type component (fwhm ≈81 kHz) is characteristic of water molecules immobilized at the inner pore surfaces. Its fwhm is roughly three times broader than that of the framework matching the expected ratio ≈ $(d_{HH}(SPAF\text{-}2)/d_{HH}(H_2O))^3$ with $d_{HH}(H_2O)$ ≈ 1.6 Å. The narrow and temperature dependent Lorentzian-type component results from mobile H_2O/H_3O^+ within the pores, which show fast and almost isotropic reorientation. It narrows with the temperature suggesting that the reorientation becomes faster (Figures S22−S24 and Table S22).

In contrast, the fwhm of the broad Gaussian-type resonance does not change markedly, indicating that water molecules attached to the inner surfaces remain immobile. With increasing temperature, the fraction of the narrow component grows at the expense of the broad component, indicating that the mobile water fraction grows. For SPAF-$2_{0.8}$ and SPAF-$2_{0.5}$, roughly 45% of the H_2O/H_3O^+ are immobilized at 220 K, while already 90% of the water molecules move isotropically at 273 K (Figure 3B). Beyond 300 K, the broad Gaussian-component falls below the detection limit. For SPAF-$2_{0.3}$, where less water is adsorbed, the proportion of the broad Gaussian-component approaches zero already beyond 250 K. Based on the DSC experiments (Figure S5 and Table S8) a small part (<15%) of the water molecules might additionally be immobilized as ice inclusions below 260 K. As this does not change the trend of the line shape analysis we omitted the contribution for the following discussion.

This analysis suggests that two water fractions, which are well distinguished in terms of mobility, coexist inside the framework. The temperature dependence of the corresponding fractions is typical for these two ensembles to be in equilibrium. Thus, for the ^1H proportions for mobile ($p(H_2O_{mo})$) and immobile ($p(H_2O_{im})$) water molecules, it follows:

$$p(H_2O_{im}) = 1 - p(H_2O_{mo}) - p(\text{framework})$$

$$p(H_2O_{mo}) = \frac{1 - p(\text{framework})}{1 + e^{\Delta H^\circ/RT}\cdot e^{-\Delta S^\circ/R}} \quad (1)$$

p(framework) is the framework proportion and ΔH^0 and ΔS^0 are the enthalpy and entropy changes. Fitting the fractions displayed in Figure 3B with eq 1 revealed that the subensemble of immobile H_2O/H_3O^+ is energetically favored by 15 to 25 kJ mol^{-1} compared to the mobile species, while the entropy for the immobile species is lower by 80−110 J mol^{-1} K^{-1} (Table S23). Due to the low contributions of the immobile species for SPAF-$2_{0.3}^{100}$ for the corresponding refinement, ΔS^0 was restricted to an average of 90 J mol^{-1} K^{-1}. We attribute the lower enthalpy for the immobilized H_2O/H_3O^+ species to attractive interactions with the SO_3^- groups. The higher entropy of the mobile fractions accounts for the higher motional degrees of freedom and an increasing disorder.

^1H NMR SFG spectroscopy allows for probing the diffusivity and thus the long-range transport of the mobile subensemble. Considering that compared to each acidic proton from a sulfonic acid group, 10−14 water molecules are adsorbed depending on x, the ^1H SFG NMR spectroscopic signal is dominated by the diffusion of adsorbed water molecules. As the spin−lattice relaxation (Figure S28) is very short (400 $\mu s \leq T_1 \leq 1$ ms), we could collect reliable ^1H SFG NMR data only for SPAF-$2_{0.3}^{100}$ and SPAF-$2_{0.8}^{100}$ (Figure 3C). In both cases, intriguingly large values of the self-diffusion coefficients D were observed, which are almost 2 orders of magnitude larger than those of water in other porous materials with similar pore sizes[44,67] and only 1 order of magnitude lower than those of liquid bulk water.[66] We attribute this to the framework's open, interconnecting 3D pore space,[32,53] which allows for unhindered diffusion despite the narrow pore sizes. The confined nature of the water molecules, nevertheless, becomes obvious considering the larger activation barriers (27 kJ $mol^{-1} \leq E_A \leq 33$ kJ mol^{-1}) compared to those of bulk water.

Further insight was obtained from ^1H spin−lattice relaxation data. The magnetization recovery is biexponential for SPAF-$2_{0.3}^{100}$, SPAF-$2_{0.5}^{100}$, and SPAF-$2_{0.8}^{100}$ for all temperatures. This makes a significant contribution from ice inclusions below 260 K unlikely (Figures S25−S27). The proportions of both components rather match the ratio for protons of the framework and adsorbed aqueous phase (Figure S29). The framework T_1 is a few tens of milliseconds and hardly temperature dependent (Figure S28). T_1 for the aqueous phase exhibits minima at 290 K (SPAF-$2_{0.8}$), 295 K (SPAF-$2_{0.5}$), and 320 K (SPAF-$2_{0.3}$), indicating dynamics on the nanoseconds scale ($\approx 1/\omega_0$) at these temperatures. However, the remarkably short T_1 values between 400 μs and 1 ms cannot be explained based on the $^1H-^1H$ dipolar coupling constants of water molecules (≈80 kHz) as derived from the line shape analyses (Figure 3A). To match the T_1 minima, 10 times larger coupling constants are required, which is unrealistic based on nuclear spin interactions.[68]

Considering, that small contents of oxidized Pd and Fe impurities are trapped in the framework (Table 1), it is likely that the spin−lattice relaxation is driven by heteronuclear dipole interactions between these paramagnetic centers and the protons of mobile H_2O/H_3O^+. In this case, T_1 exclusively probes their short-range translational motion with respect to these centers,[69] which we describe using the hydrodynamic force-free hard sphere (FFHS) model.[70] Further details are given in the Supporting Information. The FFHS model yields a spectral density $J_{trans}(\omega,\tau_{trans})$ (eq S4), which describes the fluctuations of the dipole interactions caused by the translational motion and involves a coupling constant C, which depends on the number density N_S of the paramagnetic centers, their spin state S, and the shortest possible distance d between paramagnetic centers and water molecules. In this case, T_1 is given by

$$\frac{1}{T_1} = C\cdot J_{trans}(\omega_I, \tau_{trans}) \quad (2)$$

Modeling the spin−lattice relaxation data (Figure S28 and Table S24) with eq 2 allowed us to determine the temperature-dependent correlation times τ_{trans} (Figure 3D) for all three samples. The trends for τ_{trans} suggest thermally activated translational motion with similar E_A values between 33 and 35 kJ mol^{-1} for H_2O/H_3O^+ for all SPAF-2_x. These values are in excellent agreement with E_A derived from the diffusion data, confirming that T_1 relaxation and SFG NMR spectroscopy both probe water self-diffusion. The mean distance $\langle r\rangle = \sqrt{6D\tau_{trans}}$ (Figure 3C inset), thus decodes the length scale over which a water molecule diffuses before losing the correlation to a paramagnetic center. <r> is hardly temperature-dependent and varies between 2 nm (SPAF-$2_{0.8}$) and 5 nm (SPAF-$2_{0.3}$). The somewhat larger correlation length for SPAF-$2_{0.3}$ is reflected in a larger τ_{trans} compared to SPAF-$2_{0.5}$

https://doi.org/10.1021/jacs.3c09257
J. Am. Chem. Soc. 2023, 145, 27563−27575

and SPAF-$2_{0.8}$, which show almost identical τ_{trans}. For a closed packing for the centers $N_S = 4(\sqrt{2}\langle r\rangle)^{-3}$, $\langle r\rangle \approx 3.5$ nm corresponds to a number density of 3×10^{25} m^{-3}. This matches well the observed Pd and Fe contents (Table 1), strengthening our ansatz to describe T_1 by fluctuations of heteronuclear dipole interactions caused by diffusing H_2O/H_3O^+ groups along the paramagnetic centers in the framework.

Conduction Mechanism. Using τ_{trans} and $\langle r\rangle$ (Figure 3C,D), we predict self-diffusion coefficients $D = \langle r\rangle^2 (\tau_{trans} \cdot 6)^{-1}$ for SPAF-$2_{0.5}$, where the spin−lattice relaxation was too fast to perform SFG NMR experiments. Thus, temperature-dependent D_σ could be derived for SPAF-$2_{0.3}^{100}$, SPAF-$2_{0.5}^{100}$ and SPAF-$2_{0.8}^{100}$. Applying the Nernst−Einstein relation $\sigma_x^{NMR} = n_x \cdot e^2 \cdot D\ (k_B \cdot T)^{-1}$ allows for predicting conductivities based on the temperature-dependent diffusion coefficients for SPAF-$2_{0.3}^{100}$, SPAF-$2_{0.5}^{100}$ and SPAF-$2_{0.8}^{100}$. The corresponding proton number densities n_x are given in Table S25.

The values of σ_x^{NMR} and σ_x^{EIS} match well (Figure 4A). As the ^{1}H SFG and T_1 data are mainly sensitive to the diffusion of the water molecules, this suggests that protons are carried by water molecules according to a vehicle mechanism. Despite the high IECs, this observation rules out a packed acid mechanism, where charge transport is mediated by H^+ hopping between neighboring SO_3^- units without significant water transport.[20] As T_1 relaxation, SFG NMR and EIS probe translational motion on length scales ranging from a few nanometers up to a few micrometers, the transport mechanism is length scale independent. This renders the influence of bottleneck effects unlikely.

However, while similar E_A of about 35 kJ mol^{-1} were found for $\sigma_{0.5}^{NMR}$ and $\sigma_{0.5}^{EIS}$, the activation barriers of $\sigma_{0.3}^{EIS}$ and $\sigma_{0.8}^{EIS}$ are roughly twice as high compared to the ones derived from $\sigma_{0.3}^{NMR}$ and $\sigma_{0.8}^{NMR}$ (Figure 4B). For the latter two compounds, $\sigma_x^{EIS} < \sigma_x^{NMR}$ at low temperatures, while the opposite trend is established above ≈320 K (SPAF-$2_{0.8}^{100}$) and ≈350 K (SPAF-$2_{0.3}^{100}$). H^+ transport exceeding the diffusivity of water molecules might hint toward contributions of a Grotthuss-like mechanism.[19] However, the high E_A for σ_x^{EIS} and the strong confinement by the framework make this unlikely. The small pore size suppresses the necessary formation of Zundel and Eigen ions, as water molecules within three solvation shells around one oxonium ion need to be positioned and aligned.[22]

Considering the results of the ^{1}H NMR analysis, an alternative scenario is much more likely. Confining H_2O and H_3O^+ within the framework led to the formation of two subensembles (Figure 3A,B). In addition to water molecules and oxonium ions that are immobilized in the vicinity of the SO_3^- groups, highly mobile species were observed even at temperatures far below RT (Figure 4C). The temperature dependence of their proportions revealed similar energetic differences of about 20 kJ mol^{-1} for all sulfonation degrees (Table S23). As the immobile and mobile species are spatially close and both subensembles relax with the same T_1 component (Figures S25−S27), we expect a continuous exchange of H_2O and H_3O^+ between both subensembles (Figure 4C). Water molecules and oxonium ions, immobilized at a particular time, will become mobile, or vice versa. The corresponding exchange rates κ are on the order of 10^4 Hz, as κ is small enough ($<10^6$ Hz) for the line shape analyses to be in the slow exchange limit and large enough ($>1/T_1 \approx 10^3$ Hz) to allow both subensembles to relax with the same spin−lattice relaxation rate. Due to exchange between both subensembles,

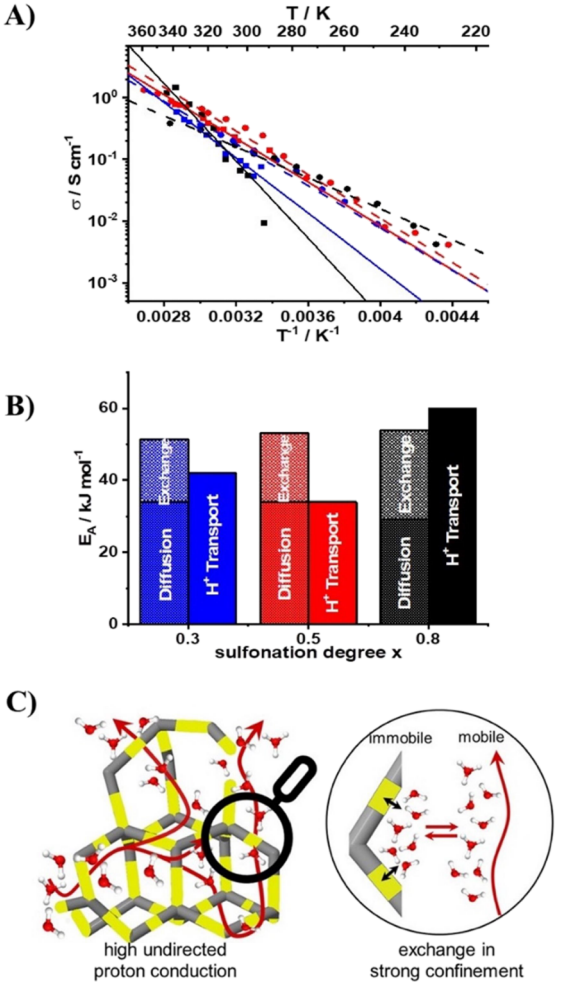

Figure 4. (A) Comparison of proton conductivities σ for SPAF-$2_{0.3}^{100}$ (blue), SPAF-$2_{0.5}^{100}$ (red), and SPAF-$2_{0.8}^{100}$ (black). Solid squares are used for data obtained with EIS. σ values derived from the ^{1}H SFG NMR (x = 0.3 and 0.8) and T_1 relaxation data (x = 0.5) using the Nernst−Einstein relation are depicted as solid circles. The lines (dashed for σ_x^{NMR} and solid for σ_x^{EIS}) are guides for the eye. (B) Comparison of activation barriers derived from the NMR spectroscopy and EIS data. (C) Schematic representation of a cutout of the molecular structure of SPAF-2_x using an ideal diamond lattice. The yellow areas symbolize hydrophilic regions around the SO_3^- units, and the gray areas represent hydrophobic regions. Zoom: Schematic presentation of the proposed mechanism for the charge transport for SPAF-$2_{0.5}^{100}$, which involves an exchange between mobile and immobilized water molecules.

the total activation barrier for the charge transport is the sum of the exchange enthalpy and the activation barrier for the diffusion (Figure 4B).

Thus, the proposed H^+ transport mechanism is a combination of periods where fast transport by diffusion occurs and periods where the same water molecules and oxonium ions become reversibly attached to the framework by electrostatic interactions (Figure 4C). The continuous exchange between two distinct, in terms of enthalpy and entropy well separated, aqueous regions sets the H^+ transport in SPAF-2_x^{100} apart from other materials like Nafion and sulfonated mesoporous silica[11,21,27] where usually homogeneous models with distributions of activation barriers apply. We attribute this difference to the strong confinement effects imposed on the aqueous phase by the narrow micropores. Due

https://doi.org/10.1021/jacs.3c09257
J. Am. Chem. Soc. 2023, 145, 27563−27575

to the 3D framework with its interpenetrating, windowless pore space, the slowdown of molecular diffusion, which usually results from strong confinement, is prevented. Despite the larger pore volumes water diffusion is slower by up 3 orders of magnitude for porous materials mentioned earlier.[11,21,27] Combining the extraordinary diffusivity within the confined aqueous phase of SPAF-2_x^{100} with IECs up to 5.7 mequiv g^{-1} and the exchange between framework-attached and free H_2O/H_3O^+ species allows for excellent conductivities between 0.5 and 2.0 S cm^{-1} (Figures 2C and 4A).

The trends for E_A as a function of the sulfonation degree determined from σ_x^{EIS} and the NMR experiments (Figure 4B) suggest that the framework polarity influences the exchange process. For x = 0.3 and 0.8, water molecules and oxonium ions participate in the exchange, as E_A determined for the charge transport (EIS) is significantly higher than E_A of the diffusion and T_1 data. In contrast, for x = 0.5, both E_A match, suggesting that only water molecules are immobilized at the SO_3^- groups, while the oxonium ions remain preferentially in the mobile phase.

We attribute this phenomenon to the distribution of sulfonic acid groups as the hydrophobic framework becomes hydrophilic in the vicinity of the SO_3^- units. Additionally, the induced electrostatic interactions provide the necessary restraint for immobilizing H_2O/H_3O^+. To probe repeating, characteristic distances, wide-angle X-ray scattering (WAXS) experiments were carried out in a Q range that corresponds to distances between 1.7 and 7.4 Å (Figure 5). As the frameworks swell upon water uptake influencing the alignment of the framework racks, the measurements were carried out in conditions where the water uptake could be controlled. Since the adsorbed water molecules are mobile and distributed in the pores, they will lead to smooth and slowly modulating scattering intensities. Sharper modulations can be attributed to the framework and the sulfonic acid groups. The diffractograms are similar for SPAF-$2_{0.3}^{100}$ and SPAF-$2_{0.8}^{100}$, with distances around 5 Å occurring most frequently (Figure 5). Such distances match those of SO_3^- groups and neighboring benzene rings. For SPAF-$2_{0.5}^{100}$, a prominent maximum of around 3.3 Å instead occurs, hinting at SO_3^- groups attached predominantly to the sandwiched benzene rings. This indicates a higher order for medium SO_3H contents.

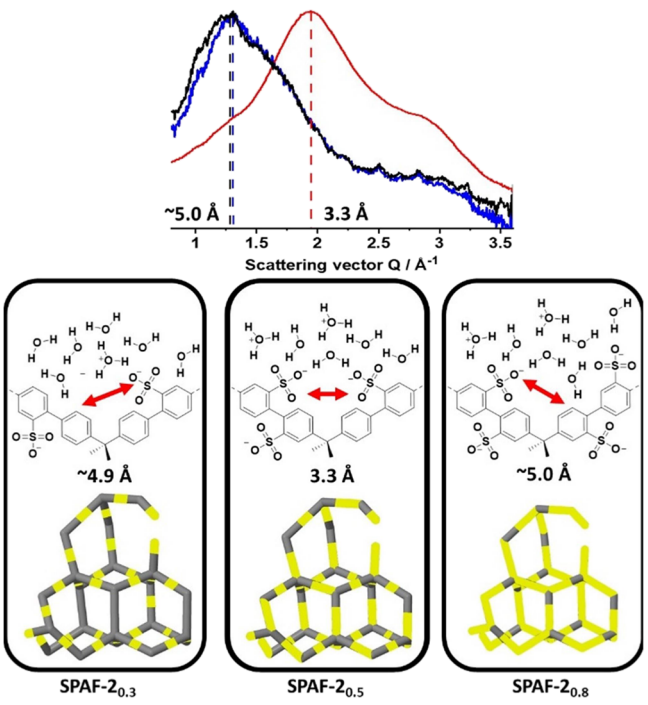

Figure 5. Top: WAXS measurement of SPAF-$2_{0.3}^{100}$ (blue), SPAF-$2_{0.5}^{100}$ (red), and SPAF-$2_{0.8}^{100}$ (black) with vertical lines highlighting the most frequently occurring distances. Deconvolutions are given in Figure S30. Schematic representation of a likely local structural arrangement of SPAF-2_x. The yellow areas symbolize hydrophilic regions around the SO_3^- units, and the gray areas represent hydrophobic regions. The red arrows point to typical framework distances that match the experimentally observed ones.

For sulfonation degrees of 0.3, 0.5, and 0.8, on average, two, three, and five of the six benzene rings of the repeating unit are sulfonated. Larger patches of unsulfonated and, thus, hydrophobic regions remain for x = 0.3 (Figure 5). For x = 0.8, almost the whole framework is hydrophilic. In both cases, the interpretation of the WAXS data suggests a disordered arrangement of sulfonate groups as the dominating peak is explained well with the framework—SO_3^- contacts. For x = 0.5, the SO_3^- groups are preferentially attached to the middle benzene units of the racks. This leads to alternating hydrophobic and hydrophilic regions (Figure 5) and might be a consequence of the Coulomb repulsion between the negatively charged SO_3^- units and the reversibility of sulfonation during synthesis.

A regular placing of SO_3^- units for x = 0.5 (Figure 5) leads to mean O−O distances that selectively attract water molecules in double hydrogen bonds, while oxonium ions do not match. This provides a reasonable explanation for the preferential immobilization of water molecules and lower activation barriers ($E_A \approx$ 35 kJ/mol) for the charge transport in this case. For x = 0.3 and 0.8, unspecific adsorption takes place which influences both water molecules and oxonium ions alike. Optimal proton conductivities are a subtle trade-off between surface interactions, water uptakes, and proton densities where optimal conditions are reached for medium-high sulfonation degrees around x = 0.5.

CONCLUSIONS

We report the synthesis and characterization of SPAF-2_x. It is a flexible, amorphous, and nanoporous framework that can be prepared with varying sulfonation degrees x. The prepared systems (x = 0.3, 0.5, and 0.8) take up roughly their own weight in water when saturated at 100% RH. More than 85% of the adsorbed water molecules are located in micropores, which induces strong confinements for the adsorbed fluid phase. Strong interactions with covalently bound SO_3^- units and IECs up to 5.7 mequiv g^{-1} promise highly efficient electrolyte-host systems with an improved water management toward higher temperatures and less hindrance due to ice formation below 0 °C.

Outstanding DC conductivities of about 1 S cm^{-1} could be realized for systems saturated at 100% RH, which surpass conductivities reported in related frameworks with similar pore sizes by 1−2 orders of magnitude (Table S1). Bulk and grain boundary transport become indistinguishable which we attribute to the formation of a continuous fluid phase including pore and particle-surface water. Although similar proton conductivities were found for low (x = 0.3), medium (x = 0.5), and high (x = 0.8) sulfonation degrees at elevated temperatures (≈353 K), the activation barriers of the charge

https://doi.org/10.1021/jacs.3c09257
J. Am. Chem. Soc. 2023, 145, 27563−27575

transport vary. Minimal values at medium sulfonation degrees provide the broadest temperature range for application as high-performance electrolyte-host material. This makes SPAF-$2^{100}_{0.5}$ promising for fabricating proton-conducting membranes used at variable temperatures between 233 and 353 K. In this range, proton conductivities vary between 0.01 and 1 S cm^{-1}.

The underlying transport processes are based on a vehicle mechanism with exceptionally high self-diffusion coefficients of about 10^{-9} m^2 s^{-1} for water molecules adsorbed in the nanometer-sized pores at RT. This surpasses the diffusivity in common micro- and mesoporous systems by up to 3 orders of magnitude. We explain this result by the open, windowless 3D pore structure of the SPAF-2 frameworks, enabling an almost unhindered diffusion despite strong confinement. The highly mobile water molecules and oxonium ions are in a continuous exchange with counterparts that strongly interact with the SO_3^- units of the framework. Water molecules and oxonium ions in this subensemble exhibit a reduced mobility and lower energy compared to those in the mobile subensemble that hardly interacts with the framework. Both subensembles are in thermal equilibrium and exchange water and oxonium ions on the order of milliseconds. When the temperature is increased, the high-energy population grows at the expense of the low-energy population, and hence, a larger number of molecules has enough thermal energy to take part in the charge and mass transport. The higher local order for the distribution of sulfonate groups for medium sulfonation degrees intriguingly leads to preferential immobilization of water molecules while the oxonium ions remain in the fluid phase. This reduces the transport barriers as oxonium ions are less likely immobilized at the framework, extending the temperature range where SPAF-$2^{100}_{0.5}$ exhibits high proton conductivities.

We show how the strong confinements imposed by nanoporous hosts on the imbedded electrolyte phase fundamentally change the mechanisms for mass and charge transport. Despite the additional restraints imposed by strong confinement, we demonstrate that it can positively impact and improve the conductivity. Maximizing the sulfonate density and IEC is less important than maximizing the framework topology, the host−guest interactions, and the sulfonate arrangement. This knowledge will help to tailor porous polymers and COFs for electrolyte-host systems with liquid-like conductivities in the future.

EXPERIMENTAL SECTION

All chemicals and solvents used in the synthesis were commercially available and were of reagent grade without further purification. Air-sensitive reactions were carried out under Ar (purity 5.0) atmosphere which passed a zeolite, P_2O_5, and BTS catalyst column. The syntheses of TPM, BrTPM, PAF-2, and SPAF-2_x are described in detail in the Supporting Information. To load the SPAF-2_x frameworks with a controlled water amount, the samples were equilibrated for up to 48 h in a humidity chamber at 33, 67, and 100% RH, respectively, using saturated salt solutions or water. Further activation was not necessary.

Physisorption measurements with Ar as absorbance were carried out on an Autosorb I at 87 K. Water physisorption measurements were performed on an ASiQ-MP-MP-AG setup (Anton Paar QuantaTec, BoyntonBeach, USA) at 293 K. Before the measurements, all samples were degassed at 393 K for 12 h. The software package ASIQ ver. 3.0 was used for data analysis. The ^1H and ^{13}C liquid-NMR spectra of the synthesized molecules were measured on a Bruker 500 MHz spectrometer and using dimethyl sulfoxide as solvent. IR spectra were recorded on a JASCO FT/IR-6100 Fourier-transform IR spectrometer with an attenuated total reflectance unit. CHNS analysis was measured on an ELEMENTAR UNICUBE with sulfanilamide as standard.

For DSC, the samples were saturated at 33, 67, and 100% RH. The measurements were done on a TA Instruments Discovery DSC 2500. The temperature range was 193 to 353 K with 5 K min^{-1} under a nitrogen atmosphere and three heating cycles. For evaluation, the third cycle was used. TGA was carried out on a Mettler Toledo TGA/SDTA851e under a nitrogen atmosphere in the temperature range from 303 to 973 K with a heating rate of 10 K min^{-1}. TGA-MS was performed on a Netzsch STA 449 C (TGA) with a Netzsch Aeolos QMS 403C (MS) under a nitrogen atmosphere with a heating rate of 5 K min^{-1}. To determine the sulfonation degree the samples were titrated with a Mettler Toledo seven2go pH meter and an aqueous 10 mM NaOH solution.

Powder X-ray diffraction was done on a STOE STADI P diffractometer with a Ge(111)monochromator and Cu−$K_{\alpha 1}$ radiation. The frameworks were packed in 1.0 mm capillaries and were measured at RT in Debye−Scherrer geometry. WAXS measurements were performed using a Xeuss 3.0 (Xenocs, France) equipped with a copper source (λ = 1.5418 Å). Scattering images were detected on an Eiger2 R 1 M detector (Dectris, Switzerland) with 1028 × 1062 pixels and a pixel size of 75 μm × 75 μm located 0.3 m from the sample (deducted via AgBeh calibration). The beam size was 0.5 mm × 0.5 mm. Each sample was equilibrated at 100% RH, sealed Kapton containers, and measured for 1 h. The WAXS images were radially averaged to extract 1D cuts and background corrected (empty container). Peak positions were determined by fitting each peak profile with a local background and a Gaussian function using XSACT 2.0 (Xenocs, France).

All solid-state NMR spectra were recorded on a Bruker Avance III HD spectrometer with a B_0 field of 9.4 T. ^1H and ^{13}C MAS spectra were performed with a ramped cross-polarization experiment in which the nutation frequency ν_{nut} on the proton channel was varied linearly from 70 to 100%. The sample was rotated with a frequency of 12.5 kHz (^{13}C) in a 3.2 mm MAS double-resonance probe (Bruker). The corresponding ν_{nut} values on the ^{13}C channel and the contact time were set to 70 kHz and 1.0 ms, respectively. Proton broadband decoupling with Spinal-64 and ν_{nut} = 60 kHz was performed during acquisition. ^{13}C spectra were referenced to tetramethylsilane using adamantane as a secondary standard. Single-pulse experiments were performed with a single 90° pulse. The pulse length was 3.20 μs, and the recycle delay was set to 120 s. The spin−lattice relaxation was characterized using an inversion recovery sequence with a leading 180° pulse of 3.5 μs.

In the ^1H SFG NMR experiments, the magnetic field gradient g was generated by a specially designed magnet with superconducting coils in anti-Helmholtz arrangement.[71] We placed the sample at a position with an ^1H Larmor frequency of 173 MHz and used two gradients of magnetic field G = 132 T m^{-1} and g = 76 T m^{-1}. The stimulated-echo sequence, which features two evolution times t_e separated by a mixing time t_m, was applied to measure the ^1H self-diffusion coefficients D. Explicitly, the stimulated-echo-decays were fitted to

$$S(t_m,t_e) \propto e^{-Dq^2t_d} \quad (3)$$

Here, $t_d = t_m + 2/3\ t_e$ is the variable diffusion time, and $q = g\gamma t_e$ with γ being the gyromagnetic ratio. The length of the 90° pulses was 0.7 μs. In all measurements, the temperature was set with an accuracy of ±1 K and stabilized to ±0.1 K using a nitrogen flow cryostat.[71]

For the conductivity measurements, the sample was placed in the sample holder under continuous gas flow with the set humidity of 33, 67, or 100% RH. For comparison a set of dried samples was immersed in liquid water. The water amount was estimated based on physisorption (Figure 1A) for p/p_0 = 1 allowing for an excess of 10%. After immersion, excess water was evaporated at room temperature against air. The water loss was controlled on a scale. When the weight was reached, the samples were sealed and equilibrated for an additional 3 days. Impedance spectroscopy was performed on a Novocontrol Alpha Analyzer with ZG4 and a 5 mV AC voltage was applied. An impedance data set was prepared to

https://doi.org/10.1021/jacs.3c09257
J. Am. Chem. Soc. 2023, 145, 27563−27575

measure the frequency range from 4 MHz to 1 Hz. To ensure the same shape and size of the pellet during measurement, the sample was placed in a cylindrical border with an active radius of 4 mm. Two copper electrodes were placed adjacent to the top and bottom of the pellet and with constant pressure of about 200 bar. The atmosphere was stable to the set value during the measurement. To ensure equilibration of the temperature, the conductivity measurement was started 30 min after the appropriate temperature. After the measurements had been made, the length (l) of the pellet was measured. From the determined lengths and $A = \pi r^2$ with $r = 4$ mm, the conductivity was calculated according to the formula $\sigma = l(A \cdot R)^{-1}$, where R is the resistance from the high-frequency semicircle in the corresponding Nyquist plot (Cole plot). This was simulated with an equivalent circuit diagram consisting of at least one resistor R and a constant phase element connected in parallel in RelaxIS 3.

■ ASSOCIATED CONTENT

Supporting Information

The Supporting Information is available free of charge at https://pubs.acs.org/doi/10.1021/jacs.3c09257.

Proton conductivities of similar porous materials for comparison, synthesis protocols, additional information on framework characterization including, elementary analysis, titration curves, EDX, TGA, IR and NMR spectroscopy, pore size distributions for PAF-2 and SPAF-2$_x$, DSC thermograms for SPAF-2$_x^{RH}$, EIS spectra and refinement parameters, ^{1}H line shape analyses, T_1 relaxation data and refinement parameters, WAXS data, and deconvolution (PDF)

■ AUTHOR INFORMATION

Corresponding Author

Jürgen Senker − *Inorganic Chemistry III and Northern Bavarian NMR Centre, University of Bayreuth, 95447 Bayreuth, Germany;* orcid.org/0000-0002-7278-7952; Email: Juergen.senker@uni-bayreuth.de

Authors

Simon F. Winterstein − *Inorganic Chemistry III and Northern Bavarian NMR Centre, University of Bayreuth, 95447 Bayreuth, Germany;* orcid.org/0000-0002-0995-042X

Alexei F. Privalov − *Institute for Condensed Matter Physics, Technical University of Darmstadt, 64289 Darmstadt, Germany;* orcid.org/0000-0002-1421-8428

Christopher Greve − *Dynamics and Structure Formation, University of Bayreuth, 95447 Bayreuth, Germany;* orcid.org/0000-0001-5506-9695

Renée Siegel − *Inorganic Chemistry III and Northern Bavarian NMR Centre, University of Bayreuth, 95447 Bayreuth, Germany;* orcid.org/0000-0003-1412-5237

Björn Pötzschner − *Inorganic Chemistry III and Northern Bavarian NMR Centre, University of Bayreuth, 95447 Bayreuth, Germany*

Michael Bettermann − *Inorganic Chemistry III and Northern Bavarian NMR Centre, University of Bayreuth, 95447 Bayreuth, Germany*

Lea Adolph − *Inorganic Chemistry III and Northern Bavarian NMR Centre, University of Bayreuth, 95447 Bayreuth, Germany*

Jana Timm − *Physical Chemistry III, Department of Chemistry, University of Bayreuth, 95447 Bayreuth, Germany*

Roland Marschall − *Physical Chemistry III, Department of Chemistry, University of Bayreuth, 95447 Bayreuth, Germany*

Ernst A. Rössler − *Inorganic Chemistry III and Northern Bavarian NMR Centre, University of Bayreuth, 95447 Bayreuth, Germany;* orcid.org/0000-0001-5586-973X

Eva M. Herzig − *Dynamics and Structure Formation, University of Bayreuth, 95447 Bayreuth, Germany;* orcid.org/0000-0002-0151-5562

Michael Vogel − *Institute for Condensed Matter Physics, Technical University of Darmstadt, 64289 Darmstadt, Germany;* orcid.org/0000-0003-2706-3522

Complete contact information is available at: https://pubs.acs.org/10.1021/jacs.3c09257

Author Contributions

$^\perp$In memoriam to our dear colleague; unexpectedly deceased on November first 2022.

Author Contributions

The manuscript was written with the contributions of all authors. All authors have approved the final version of the manuscript.

Funding

This project was funded by the DFG, project number 492723217 (CRC 1585), the University of Bayreuth, and the Technical University of Darmstadt.

Notes

The authors declare no competing financial interest.

■ ACKNOWLEDGMENTS

Financial support by the DFG, Project number 492723217 (CRC 1585) subprojects A01, A04, and B03 is gratefully acknowledged. We thank Profs. Josef Breu, Markus Retsch, and Birgit Weber for access to Ar physisorption and thermal and elementary analysis. Furthermore, we are grateful to Beate Bojer, Marco Schwarzmann, and Sonja Lutschinger for collecting the ^{1}H and ^{13}C MAS NMR spectra and acquiring SEM images. We thank Dr. Ulrich Mansfeld for performing ESEM measurements.

■ ABBREVIATIONS

PMFC	polymer membrane fuel cell
MEA	membrane electrolyte assembly
IEC	ion exchange capacity
RH	relative humidity
POM	polyoxometalate
MOF	metal−organic framework
POF	porous organic framework
PAF	porous aromatic framework
SPAF	sulfonated porous aromatic framework
FTIR	Fourier-transform infrared
NMR	nuclear magnetic resonance
EA	elemental analysis
EDX	energy-dispersive X-ray
TGA	thermal gravimetric analysis
DSC	differential scanning calorimetry
BrTPM	tetrakis(4-bromophenyl)methane
BDB	benzene-1,4-diboronicacid
SP	single-pulse
BET	Brunauer−Emmett−Teller
TGA-MS	thermal gravimetric analysis mass spectrometry
SA	surface area

DFT	density functional theory
IUPAC	international union of pure and applied chemistry
ESEM	environmental scanning electron microscope
EIS	electrochemical impedance spectroscopy
B	bulk
GB	grain boundaries
E	electrode
EI	electrode interface
fwhm	full widths at half-maximum
SFG	static-field gradient
DC	direct current
WAXS	wide-angle X-ray scattering
FFHS	force-free hard sphere

REFERENCES

(1) Basu, S. *Recent Trends in Fuel Cell Science and Technology*; Basu, S., Ed.; Springer New York: New York, NY, 2007; pp 1−3.
(2) Larminie, J.; Dicks, A. *Fuel Cell Systems Explained*; Wiley: West Sussex, England, 2003; pp 72−75.
(3) Peighambardoust, S. J.; Rowshanzamir, S.; Amjadi, M. Review of the Proton Exchange Membranes for Fuel Cell Applications. *Int. J. Hydrogen Energy* **2010**, *35*, 9349−9384.
(4) Kreuer, K. D. On the Development of Proton Conducting Polymer Membranes for Hydrogen and Methanol Fuel Cells. *J. Membr. Sci.* **2001**, *185*, 29−39.
(5) Mauritz, K. A.; Moore, R. B. State of Understanding of Nafion. *Chem. Rev.* **2004**, *104*, 4535−4585.
(6) Souzy, R.; Ameduri, B.; Boutevin, B.; Gebel, G.; Capron, P. Functional Fluoropolymers for Fuel Cell Membranes. *Solid State Ionics* **2005**, *176*, 2839−2848.
(7) Gubler, L.; Gürsel, S. A.; Scherer, G. G. Radiation Grafted Membranes for Polymer Electrolyte Fuel Cells. *Fuel Cells* **2005**, *5*, 317−335.
(8) de Bruijn, F. A.; Makkus, R. C.; Mallant, R. K. A. M.; Janssen, G. J. M. Materials for State-of-the-Art PEM Fuel Cells, and Their Suitability for Operation Above 100°C. In *Advances in Fuel Cells*; Elsevier Science, 2007; Vol. *1*, pp 235−336.
(9) Kreuer, K. D.; Paddison, S. J.; Spohr, E.; Schuster, M. Transport in Proton Conductors for Fuel-Cell Applications: Simulations, Elementary Reactions, and Phenomenology. *Chem. Rev.* **2004**, *104*, 4637−4678.
(10) Keerthi, A.; Goutham, S.; You, Y.; Lamprasertkun, P.; Dryfe, R. A. W.; Geim, A. K.; Radha, B. Water Friction in Nanofluidic Channels Made from Two-Dimensional Crystals. *Nat. Commun.* **2021**, *12*, 3092.
(11) Hammer, R.; Schönhoff, M.; Hansen, M. R. Comprehensive Picture of Water Dynamics in Nafion Membranes at Different Levels of Hydration. *J. Phys. Chem. B* **2019**, *123*, 8313−8324.
(12) Galitskaya, E. A.; Privalov, A. F.; Vogel, M.; Ryzhkin, I. A.; Sinitsyn, V. V. Self-Diffusion Micromechanism in Nafion Studied by ^{2}H NMR Relaxation Dispersion. *J. Chem. Phys.* **2021**, *154*, No. 034904.
(13) Plazanet, M.; Morfin, I.; Honkimäki, V.; Buslaps, T.; Petrillo, C.; Sacchetti, F. Hydrogen-Bond Network Distortion of Water in the Soft Confinement of Nafion Membrane. *J. Chem. Phys.* **2021**, *154*, 244503.
(14) Kreuer, K. -D; Rabenau, A.; Weppner, W. Vehicle Mechanism, A New Model for the Interpretation of the Conductivity of Fast Proton Conductors. *Angew. Chem., Int. Ed. Engl.* **1982**, *21*, 208−209.
(15) Liu, R.; Wang, D.-Y.; Shi, J.-R.; Li, G. Proton Conductive Metal Sulfonate Frameworks. *Coord. Chem. Rev.* **2021**, *431*, No. 213747.
(16) Privalov, A. F.; Galitskaya, E.; Sinitsyn, V.; Vogel, M. Isotope Effect on Diffusion in Nafion Studied by NMR Diffusometry. *Appl. Magn. Reson.* **2020**, *51*, 145−153.
(17) Sahoo, R.; Mondal, S.; Pal, S. C.; Mukherjee, D.; Das, M. C. Covalent-Organic Frameworks (COFs) as Proton Conductors. *Adv. Energy Mater.* **2021**, *11*, No. 2102300.
(18) von Grotthuss, T. *Mémoire Sur La Décomposition de l'eau et Des Corps Qu'elle Tient En Dissolution à l'aide de l'électricité Galvanique*; Rome, 1806.
(19) Ogawa, T.; Kamiguchi, K.; Tamaki, T.; Imai, H.; Yamaguchi, T. Differentiating Grotthuss Proton Conduction Mechanisms by Nuclear Magnetic Resonance Spectroscopic Analysis of Frozen Samples. *Anal. Chem.* **2014**, *86*, 9362−9366.
(20) Ogawa, T.; Aonuma, T.; Tamaki, T.; Ohashi, H.; Ushiyama, H.; Yamashita, K.; Yamaguchi, T. The Proton Conduction Mechanism in a Material Consisting of Packed Acids. *Chem. Sci.* **2014**, *5*, 4878.
(21) Sharifi, M.; Wark, M.; Freude, D.; Haase, J. Highly Proton Conducting Sulfonic Acid Functionalized Mesoporous Materials Studied by Impedance Spectroscopy, MAS NMR Spectroscopy and MAS PFG NMR Diffusometry. *Microporous Mesoporous Mater.* **2012**, *156*, 80−89.
(22) Agmon, N. The Grotthuss Mechanism. *Chem. Phys. Lett.* **1995**, *244*, 456−462.
(23) Schlick, S. *The Chemistry of Membranes Used in Fuel Cells*; Schlick, S., Ed.; Wiley: Hoboken, New York, USA, 2018; pp 6−265.
(24) Di Noto, V.; Zawodzinski, T. A.; Herring, A. M.; Giffin, G. A.; Negro, E.; Lavina, S. Polymer Electrolytes for a Hydrogen Economy. *Int. J. Hydrogen Energy* **2012**, *37*, 6120−6131.
(25) Smitha, B.; Sridhar, S.; Khan, A. A. Solid Polymer Electrolyte Membranes for Fuel Cell Applications—a Review. *J. Membr. Sci.* **2005**, *259*, 10−26.
(26) Meng, X.; Wang, H.-N.; Song, S.-Y.; Zhang, H.-J. Proton-Conducting Crystalline Porous Materials. *Chem. Soc. Rev.* **2017**, *46*, 464−480.
(27) Furtmair, M.; Timm, J.; Marschall, R. Sulfonation of Porous Materials and Their Proton Conductivity. *Microporous Mesoporous Mater.* **2021**, *312*, No. 110745.
(28) Chen, J.; Mei, Q.; Chen, Y.; Marsh, C.; An, B.; Han, X.; Silverwood, I. P.; Li, M.; Cheng, Y.; He, M.; Chen, X.; Li, W.; Kippax-Jones, M.; Crawshaw, D.; Frogley, M. D.; Day, S. J.; García-Sakai, V.; Manuel, P.; Ramirez-Cuesta, A. J.; Yang, S.; Schröder, M. Highly Efficient Proton Conduction in the Metal-Organic Framework Material MFM-300(Cr)·$SO_4(H_3O)_2$. *J. Am. Chem. Soc.* **2022**, *144*, 11969−11974.
(29) Biradha, K.; Goswami, A.; Moi, R.; Saha, S. Metal−Organic Frameworks as Proton Conductors: Strategies for Improved Proton Conductivity. *Dalt. Trans.* **2021**, *50*, 10655−10673.
(30) Xue, W.; Sewell, C. D.; Zhou, Q.; Lin, Z. Metal−Organic Frameworks for Ion Conduction. *Angew. Chem., Int. Ed.* **2022**, *61*, No. e202206512.
(31) Zhang, S.; Yang, Q.; Wang, C.; Luo, X.; Kim, J.; Wang, Z.; Yamauchi, Y. Porous Organic Frameworks: Advanced Materials in Analytical Chemistry. *Adv. Sci.* **2018**, *5*, No. 1801116.
(32) Tian, Y.; Zhu, G. Porous Aromatic Frameworks (PAFs). *Chem. Rev.* **2020**, *120*, 8934−8986.
(33) Xu, H.; Tao, S.; Jiang, D. Proton Conduction in Crystalline and Porous Covalent Organic Frameworks. *Nat. Mater.* **2016**, *15*, 722−726.
(34) Jain, S. K.; Rawlings, D.; Antoine, S.; Segalman, R. A.; Han, S. Confinement Promotes Hydrogen Bond Network Formation and Grotthuss Proton Hopping in Ion-Conducting Block Copolymers. *Macromolecules* **2022**, *55*, 615−622.
(35) Klumpen, C.; Gödrich, S.; Papastavrou, G.; Senker, J. Water Mediated Proton Conduction in a Sulfonated Microporous Organic Polymer. *Chem. Commun.* **2017**, *53*, 7592−7595.
(36) Zou, W.; Jiang, G.; Zhang, W.; Zhang, L.; Cui, Z.; Song, H.; Liang, Z.; Du, L. Hierarchically Macro−Microporous Covalent Organic Frameworks for Efficient Proton Conduction. *Adv. Funct. Mater.* **2023**, *33*, No. 2213642.
(37) Kang, D. W.; Lim, K. S.; Lee, K. J.; Lee, J. H.; Lee, W. R.; Song, J. H.; Yeom, K. H.; Kim, J. Y.; Hong, C. S. Cost-Effective, High-Performance Porous-Organic-Polymer Conductors Functionalized with Sulfonic Acid Groups by Direct Postsynthetic Substitution. *Angew. Chemie Int. Ed.* **2016**, *55*, 16123−16126.

https://doi.org/10.1021/jacs.3c09257
J. Am. Chem. Soc. 2023, 145, 27563−27575

(38) Peng, Y.; Xu, G.; Hu, Z.; Cheng, Y.; Chi, C.; Yuan, D.; Cheng, H.; Zhao, D. Mechanoassisted Synthesis of Sulfonated Covalent Organic Frameworks with High Intrinsic Proton Conductivity. *ACS Appl. Mater. Interfaces* **2016**, *8*, 18505−18512.
(39) Zhang, Y.; Li, C.; Liu, Z.; Yao, Y.; Hasan, M. M.; Liu, Q.; Wan, J.; Li, Z.; Li, H.; Nagao, Y. Intrinsic Proton Conduction in 2D Sulfonated Covalent Organic Frameworks through a Post-Synthetic Strategy. *CrystEngComm* **2021**, *23*, 6234−6238.
(40) Bhanja, P.; Palui, A.; Chatterjee, S.; Kaneti, Y. V.; Na, J.; Sugahara, Y.; Bhaumik, A.; Yamauchi, Y. Crystalline Porous Organic Polymer Bearing -SO_3H Functionality for High Proton Conductivity. *ACS Sustain. Chem. Eng.* **2020**, *8*, 2423−2432.
(41) Muriithi, B.; Loy, D. Proton Conductivity of Nafion/Ex-Situ Sulfonic Acid-Modified Stöber Silica Nanocomposite Membranes As a Function of Temperature, Silica Particles Size and Surface Modification. *Membranes (Basel).* **2016**, *6*, 12.
(42) Pereira, F.; Vallé, K.; Belleville, P.; Morin, A.; Lamberts, S.; Sanchez, C. Advanced Mesostructured Hybrid Silica-Nafion Membranes for High-Performance PEM Fuel Cell. *Chem. Mater.* **2008**, *20*, 1710−1718.
(43) Sattig, M.; Vogel, M. Dynamic Crossovers and Stepwise Solidification of Confined Water: A ^{2}H NMR Study. *J. Phys. Chem. Lett.* **2014**, *5*, 174−178.
(44) Weigler, M.; Winter, E.; Kresse, B.; Brodrecht, M.; Buntkowsky, G.; Vogel, M. Static Field Gradient NMR Studies of Water Diffusion in Mesoporous Silica. *Phys. Chem. Chem. Phys.* **2020**, *22*, 13989−13998.
(45) Jani, A.; Busch, M.; Mietner, J. B.; Ollivier, J.; Appel, M.; Frick, B.; Zanotti, J. M.; Ghoufi, A.; Huber, P.; Fröba, M.; Morineau, D. Dynamics of Water Confined in Mesopores with Variable Surface Interaction. *J. Chem. Phys.* **2021**, *154*, No. 094505.
(46) Itoh, Y.; Chen, S.; Hirahara, R.; Konda, T.; Aoki, T.; Ueda, T.; Shimada, I.; Cannon, J. J.; Shao, C.; Shiomi, J.; Tabata, K. V.; Noji, H.; Sato, K.; Aida, T. Ultrafast Water Permeation through Nanochannels with a Densely Fluorous Interior Surface. *Science (80-.)* **2022**, *376*, 738−743.
(47) Kavokine, N.; Bocquet, M. L.; Bocquet, L. Fluctuation-Induced Quantum Friction in Nanoscale Water Flows. *Nat. 2022 6027895* **2022**, *602*, 84−90.
(48) Dai, Q.; Liu, Z.; Huang, L.; Wang, C.; Zhao, Y.; Fu, Q.; Zheng, A.; Zhang, H.; Li, X. Thin-Film Composite Membrane Breaking the Trade-off between Conductivity and Selectivity for a Flow Battery. *Nat. Commun.* **2020**, *11*, 13.
(49) Li, J.; Wang, J.; Wu, Z.; Tao, S.; Jiang, D. Ultrafast and Stable Proton Conduction in Polybenzimidazole Covalent Organic Frameworks via Confinement and Activation. *Angew. Chemie Int. Ed.* **2021**, *60*, 12918−12923.
(50) Adams, E. M.; Hao, H.; Leven, I.; Rüttermann, M.; Wirtz, H.; Havenith, M.; Head-Gordon, T. Proton Traffic Jam: Effect of Nanoconfinement and Acid Concentration on Proton Hopping Mechanism. *Angew. Chemie Int. Ed.* **2021**, *60*, 25419−25427.
(51) Zelovich, T.; Winey, K. I.; Tuckerman, M. E. Hydronium Ion Diffusion in Model Proton Exchange Membranes at Low Hydration: Insights from Ab Initio Molecular Dynamics. *J. Mater. Chem. A* **2021**, *9*, 2448−2458.
(52) Rose, M.; Klein, N.; Böhlmann, W.; Böhringer, B.; Fichtner, S.; Kaskel, S. New Element Organic Frameworks via Suzuki Coupling with High Adsorption Capacity for Hydrophobic Molecules. *Soft Matter* **2010**, *6*, 3918−3923.
(53) Ben, T.; Qiu, S. Porous Aromatic Frameworks: Synthesis, Structure and Functions. *CrystEngComm* **2013**, *15*, 17−26.
(54) Thomas, J. M. H.; Trewin, A. Amorphous PAF-1: Guiding the Rational Design of Ultraporous Materials. *J. Phys. Chem. C* **2014**, *118*, 19712−19722.
(55) Fayon, P.; Trewin, A. Formation Mechanism of Ultra Porous Framework Materials. *Phys. Chem. Chem. Phys.* **2016**, *18*, 16840−16847.
(56) Thommes, M.; Kaneko, K.; Neimark, A. V.; Olivier, J. P.; Rodriguez-Reinoso, F.; Rouquerol, J.; Sing, K. S. W. Physisorption of Gases, with Special Reference to the Evaluation of Surface Area and Pore Size Distribution (IUPAC Technical Report). *Pure Appl. Chem.* **2015**, *87*, 1051−1069.
(57) Klumpen, C.; Winterstein, S.; Papastavrou, G.; Senker, J. Anhydrous Proton Conduction in Porous Organic Networks. *J. Mater. Chem. A* **2018**, *6*, 21542−21549.
(58) Schreiber, A.; Ketelsen, I.; Findenegg, G. H. Melting and Freezing of Water in Ordered Mesoporous Silica Materials. *Phys. Chem. Chem. Phys.* **2001**, *3*, 1185−1195.
(59) Geng, P.; Zore, A.; Van De Mark, M. R. Thermodynamic Characterization of Free and Surface Water of Colloidal Unimolecular Polymer (CUP) Particles Utilizing DSC. *Polymers (Basel).* **2020**, *12*, 1417.
(60) Nicotera, I.; Coppola, L.; Rossi, C. O.; Youssry, M.; Ranieri, G. A. NMR Investigation of the Dynamics of Confined Water in Nafion-Based Electrolyte Membranes at Subfreezing Temperatures. *J. Phys. Chem. B* **2009**, *113*, 13935−13941.
(61) Zawodzinski, T. A.; Derouin, C.; Radzinski, S.; Sherman, R. J.; Smith, V. T.; Springer, T. E.; Gottesfeld, S. Water Uptake by and Transport Through Nafion® 117 Membranes. *J. Electrochem. Soc.* **1993**, *140*, 1041.
(62) Fimrite, J.; Struchtrup, H.; Djilali, N. Transport Phenomena in Polymer Electrolyte Membranes. *J. Electrochem. Soc.* **2005**, *152*, A1804.
(63) Colomban, P. Proton Conductors: Solids, Membranes and Gels — Materials and Devices. In *Chemistry of Solid State Materials*; Cambridge University Press: Cambridge, 2008; Vol. 2, p 616.
(64) Colomban, P.; Novak, A. Proton Transfer and Superionic Conductivity in Solids and Gels. *J. Mol. Struct.* **1988**, *177*, 277−308.
(65) Kreuer, K.-D. Proton Conductivity: Materials and Applications. *Chem. Mater.* **1996**, *8*, 610−641.
(66) Price, W. S.; Ide, H.; Arata, Y. Self-Diffusion of Supercooled Water to 238 K Using PGSE NMR Diffusion Measurements. *J. Phys. Chem. A* **1999**, *103*, 448−450.
(67) Bourdin, V.; Germanus, A.; Grenier, P.; Kärger, J. Application of the Thermal Frequency Response Method and of Pulsed Field Gradient NMR to Study Water Diffusion in Zeolite NaX. *Adsorption* **1996**, *2*, 205−216.
(68) Steigel, A.; Spiess, H. W. Dynamic NMR Spectroscopy. In *NMR Basic Principles and Progress*; Springer Berlin Heidelberg: Berlin, Heidelberg, 1978.
(69) Albrand, J. P.; Taieb, M. C.; Fries, P. H.; Belorizky, E. NMR Study of Spectral Densities over a Large Frequency Range for Intermolecular Relaxation in Liquids: Pair Correlation Effects. *J. Chem. Phys.* **1998**, *78*, 5809.
(70) Becher, M.; Wohlfromm, T.; Rössler, E. A.; Vogel, M. Molecular Dynamics Simulations vs Field-Cycling NMR Relaxometry: Structural Relaxation Mechanisms in the Glass-Former Glycerol Revisited. *J. Chem. Phys.* **2021**, *154*, 124503.
(71) Geil, B. Measurement of Translational Molecular Diffusion Using Ultrahigh Magnetic Field Gradient NMR. *Magn. Reson.* **1998**, *10*, 299−321.

https://doi.org/10.1021/jacs.3c09257
J. Am. Chem. Soc. 2023, 145, 27563−27575